Photoinitiated H_2CO unimolecular decomposition: Accessing H+HCO products via S_0 and T_1 pathways

L. R. Valachovic,[a] M. F. Tuchler,[b] M. Dulligan,[c] Th. Droz-Georget,[d]
M. Zyrianov, A. Kolessov, H. Reisler,[e] and C. Wittig[e]
Department of Chemistry, University of Southern California, Los Angeles, California 90089-0482

(Received 18 October 1999; accepted 16 November 1999)

The photoinitiated unimolecular decomposition of formaldehyde via the H+HCO radical channel has been examined at energies where the S_0 and T_1 pathways both participate. The barrierless S_0 pathway has a loose transition state (which tightens somewhat with increasing energy), while the T_1 pathway involves a barrier and therefore a tight transition state. The product state distributions which derive from the S_0 and T_1 pathways differ qualitatively, thereby providing a means of discerning the respective S_0 and T_1 contributions. Energies in excess of the H+HCO threshold have been examined throughout the range $1103 \leqslant E^{\dagger} \leqslant 2654\,\mathrm{cm}^{-1}$ by using two complementary experimental techniques; ion imaging and high-n Rydberg time-of-flight spectroscopy. It was found that S_0 dominates at the low end of the energy range. Here, T_1 participation is sporadic, presumably due to poor coupling between zeroth-order S_1 levels and T_1 reactive resonances. These T_1 resonances have small decay widths because they lie below the T_1 barrier. Alternatively, at the high end of the energy range, the T_1 pathway dominates, though a modest S_0 contribution is always present. The transition from S_0 dominance to T_1 dominance occurs over a broad energy range. The most reliable value for the T_1 barrier ($1920 \pm 210\,\mathrm{cm}^{-1}$) is given by the recent *ab initio* calculations of Yamaguchi *et al.* It lies near the center of the region where the transition from S_0 dominance to T_1 dominance takes place. Thus, the present results are consistent with the best theoretical calculations as well as the earlier study of Chuang *et al.*, which bracketed the T_1 barrier energy between 1020 and 2100 cm^{-1} above the H+HCO threshold. The main contribution of the present work is an experimental demonstration of the transition from S_0 to T_1 dominance, highlighting the sporadic nature of this competition. © *2000 American Institute of Physics.* [S0021-9606(00)01306-4]

I. INTRODUCTION

Unraveling the photophysics and photochemistry of gas phase formaldehyde has deepened our understanding of intramolecular and reaction dynamics in small polyatomic molecules.[1–17] Because of the many desirable features of its energy level structure, as well as the vast amount of information that has accrued concerning couplings between zeroth-order levels, H_2CO is an attractive candidate for detailed studies of complex phenomena associated with S_1 radiationless decay. For example, Fig. 1 shows that several parallel unimolecular decomposition pathways exist, yielding two sets of chemically distinct products,

$$H_2CO \rightarrow H_2 + CO \quad (1)$$

$$\rightarrow H + HCO, \quad (2)$$

where reaction (1) occurs solely via S_0, while reaction (2) can occur via both S_0 and T_1.

Not only do the molecular (H_2+CO) and radical (H+HCO) product channels compete, but distinct S_0 and T_1 pathways can lead to the same products, i.e., the H+HCO channel. It is this competition within the radical channel which is the focus of the present study. The S_1-S_0 and S_1-T_1 coupling mechanisms are different, and in addition reactions that yield radical products proceed on the S_0 and T_1 surfaces via loose and tight transition states, respectively. Understanding the dynamics of such competition requires a knowledge of how the various molecular parameters influence the apportionment of reactive flux into the different decay pathways. Indeed, this is a central issue in molecular reaction dynamics.

Formaldehyde's S_1 surface is readily accessed from the S_0 vibrationless ground state via photoexcitation, which is enhanced by out-of-plane (ν_4) vibrations on S_1. The $S_1 \leftarrow S_0$ system is essentially an $\pi^* \leftarrow n$ transition localized on the CO moiety. At the energies of the low-lying S_1 vibrational levels, the manifold of T_1 vibrational levels is sparse, and therefore the dominant nonradiative pathway is internal conversion to S_0. However, as the T_1 vibrational level density increases with energy, S_1-T_1 couplings between near-isoenergetic states become more probable, thus facilitating

[a]Present address: The Aerospace Corporation, MS 5-752, P.O. Box 96957, Los Angeles, CA 90009.
[b]Present address: Department of Chemistry, Washington and Lee University, Lexington, VA 24450.
[c]Present address: AFRL/PRRS/ERC, 10 East Saturn Blvd., Edwards AFB, CA 93524.
[d]Present address: Novartis Services AG, K-127.6.78, CH-4002 Basel, Switzerland.
[e]Author to whom correspondence should be addressed. Electronic mail: reisler@chem1.usc.edu; wittig@chem1.usc.edu

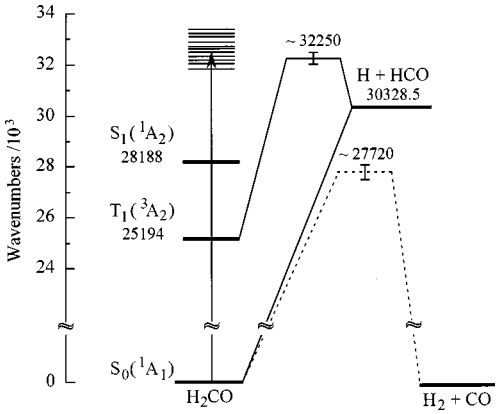

FIG. 1. Energy diagram for the lowest H_2CO dissociation channels. The T_1 barrier energy is from Ref. 23. Following $S_1 \leftarrow S_0$ photoexcitation, the $S_1 \rightarrow S_0$ and $S_1 \rightarrow T_1$ pathways both lead to H+HCO products, while H_2+CO is accessible only via $S_1 \rightarrow S_0$.

intersystem crossing. Hence, the viability of the T_1 unimolecular decomposition pathway increases with energy.

The S_1 and S_0 surfaces are coupled by second-order nonadiabatic vibronic interactions,[14] whereas the S_1 and T_1 surfaces are coupled by second-order spin–orbit interactions.[11–13,15,16] These couplings are weak. The magnitudes of the measured S_1-T_1 matrix elements range from 0.01 to 0.1 cm^{-1}.[16] The magnitudes of the S_1-S_0 matrix elements have been obtained experimentally for D_2CO, where an upper bound of less than $10^{-4}\,cm^{-1}$ has been reported.[6–8] The H_2CO matrix elements are expected to be somewhat larger.[17–19] When combined with other molecular parameters, such as level densities, these parameters can be used to estimate coupling strengths, as discussed below.

While reaction (1) has been the focus of many studies,[1,2] the mechanism of reaction (2) has received less attention. The competition between reactions proceeding on S_0 and T_1 has been examined experimentally by Chuang *et al.*,[20] who deduced that the top of the T_1 barrier lies between 1020 and 2100 cm^{-1} above the H+HCO threshold (30 328.5 cm^{-1}).[21] Dulligan *et al.* studied reaction (2) at excitation energies between 31 500 and 31 855 cm^{-1}.[22] They argued that competition between dissociation on S_0 and T_1 is important throughout this range, and that the contribution of each pathway can fluctuate strongly with excitation energy. Because of these fluctuations and the role played by tunneling, the experimental data could not be used to infer an accurate value for the energy of the T_1 barrier. A recent *ab initio* calculation by Yamaguchi *et al.* places the T_1 barrier at $1920 \pm 210\,cm^{-1}$.[23] The high accuracy of this calculation makes it the most reliable determination of the T_1 barrier energy to date. The present results complement the seminal study of Chuang *et al.*,[20] the earlier results from our group,[22] and the high-level *ab initio* calculations.[23]

In the present study, $S_1 \leftarrow S_0$ photoexcitation has been carried out by using a range of photon energies (31 431–32 983 cm^{-1}) for which it is believed that the competition between the S_0 and T_1 pathways can be most easily discerned. The region of the T_1 barrier is explored—from sufficiently below the top to ensure S_0 dominance, to sufficiently above the top to observe T_1 dominance.

The S_1-S_0 coupling matrix elements fluctuate since they depend on the nature of the S_0 levels (or resonances), which have been shown to be ergodic.[9,10] At the energies of interest, the effect of these fluctuations on the S_0 reaction rates will, to some extent, be averaged out. Note that the S_0 pathway leading to molecular products is open throughout the energy range of interest.

In contrast, the fluctuations in the T_1 rates are expected to be relatively large. The T_1 contribution to reaction (2) depends on the proximity of S_1 and T_1 levels of the same symmetry, as well as features of the T_1 surface. Indeed, the energy of the top of the T_1 barrier is critical. Below it, S_1-T_1 coupling is limited by the sparse T_1 level density and the narrow T_1 resonance widths (i.e., the T_1 reaction rates are governed by tunneling and therefore are small). Above it, the T_1 resonance widths are expected to be comparable to the mean level spacings of the T_1 levels which can be accessed from a single S_1 level. In this region the T_1 pathway may compete favorably.

The work reported herein makes use of distinct experimental signatures of the S_0 and the T_1 unimolecular decomposition pathways. Since the S_0 pathway is barrierless, the corresponding product state distributions (PSD's) are expected to be near statistical. On the other hand, the T_1 barrier results in PSD's which differ qualitatively from their S_0 counterparts, at least at the energies of concern in the present study. Specifically, it is anticipated that for the HCO produced via T_1, vibrational excitation will be scant and modest *a*-axis rotation will result in only the lowest K_a levels being populated. The utility of the S_0 and T_1 signatures derives from the fact that they are very different.

The experimental strategy, which pays special attention to the signatures mentioned above, is straightforward. A number of ''excess'' energies (i.e., in excess of 30 328.5 cm^{-1}) were chosen to lie just above the energies of low-lying HCO vibrational levels. The population of HCO vibrations at energies just above their thresholds is a signature of statistical dissociation on a barrierless surface. Rotational distributions were also determined; they provide good signatures for both the statistical (S_0) and dynamically biased (T_1) pathways. The variation in the PSD's as a function of excitation wavelength then reveals how S_0 and T_1 participation varies with excess energy.

Two complementary experimental techniques were used; photofragment ion imaging and high-*n* Rydberg time-of-flight (HRTOF) spectroscopy. Each yields center-of-mass (c.m.) translational energy distributions, which are equivalent to HCO internal energy distributions. The ion imaging arrangement is particularly sensitive to products with low c.m. translational energy, and therefore best reveals HCO vibrational populations when the excess energies are just above the thresholds for these levels. However, the resolution is low; i.e. only HCO vibrations can be resolved. With the HRTOF technique, as implemented here, only the two lowest HCO vibrational levels are seen, but the resolution is higher and partially resolved rotational structure is obtained.

The results support a mechanism in which S_0 dominance yields to T_1 dominance with increasing energy. The energy

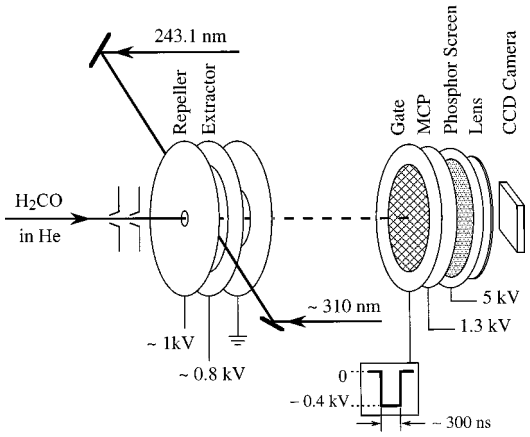

FIG. 2. Schematic of the photofragment ion imaging experimental arrangement.

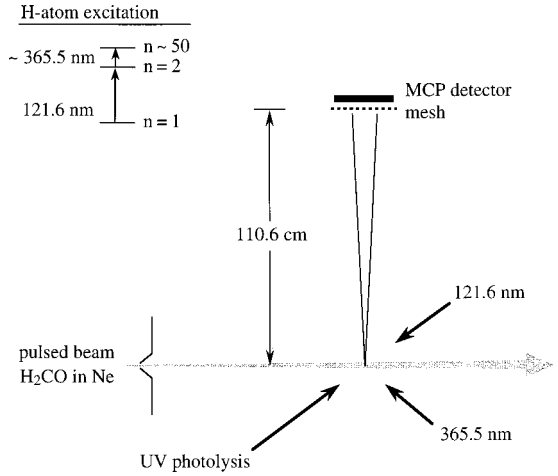

FIG. 3. Schematic of the HRTOF experimental arrangement.

range over which this transition takes place is broad and most likely centered near the top of the T_1 barrier. At the lowest photon energies used, T_1 participation is sporadic, while at the highest photon energies used, S_0 participation is persistent but is modest relative to that of T_1.

II. EXPERIMENTS

Both the photofragment ion imaging and the HRTOF techniques have been used to obtain HCO internal energy distributions following photoexcitation at various wavelengths. The ion imaging method yields two-dimensional (2D) projections of the three-dimensional (3D) distributions of H-atom velocities, whereas the HRTOF method provides angle-specific distributions of H-atom arrival times. Both techniques have the advantage that HCO internal energy *distributions* are obtained with each laser firing. However, the HRTOF technique, at least as implemented in the present study, is biased against low H-atom speeds; for example, H atoms whose recoil velocities are nearly equal to the molecular beam velocity cannot be collected because they miss the detector. On the other hand, the full range of H-atom velocities is recorded when using the imaging method, but with lower resolution. Thus, the two techniques are complementary, and consistency between the two data sets is easily verified.

A. Ion imaging

The photofragment ion imaging arrangement (Fig. 2) is standard,[24–28] and includes ion optics configured for velocity mapping.[26–28] Briefly, the apparatus consists of an ion acceleration stage (repeller, extractor, grounded plates), a 60 cm drift tube, and a position sensitive microchannel plate (MCP) detector, positioned parallel to the ion-optics plates. The MCP detector is coupled to a phosphor screen which is monitored by a CCD camera. Details are given elsewhere.[28] With this method, all ions having the same initial velocity vector are focused to the same position on the detector, but the conversion from radial distance (as measured from the center of the image) to velocity depends on the voltage ratio employed to achieve velocity focusing, and therefore must be calibrated. The projection on the detector plane is recorded as an image. Temporal gating of the detector provides mass resolution. Acceleration voltages between 35 and 95 V/cm were used, corresponding to flight times $\leqslant 2$ μs.

A pulsed, skimmed, differentially-pumped molecular beam containing $\sim 1\%$ H_2CO in He was prepared by passing He at 1 atm over paraformaldehyde heated to $\sim 90\,^{\circ}C$. The mixture then passed through a cold trap ($-95\,^{\circ}C$) prior to entering the nozzle assembly. Expansion cooled H_2CO ($T_{rot} \leqslant 6$ K) entered the reaction chamber through a 1 mm hole in the repeller plate along the symmetry axis of the ion optics, and was photoexcited by using linearly polarized, pulsed, tunable radiation (0.5–1 mJ, 304–318 nm) which was slightly defocused (15 cm focal length) in the interaction region. Nascent H atoms were probed via $2+1$ resonance-enhanced multiphoton ionization (REMPI) (Ref. 29) by using 0.2 mJ of focused (15 cm focal length) 243.1 nm radiation, which was linearly polarized in the vertical direction of the detector plane. The pump and probe beams counterpropagated along a direction perpendicular to the molecular beam axis with a pump–probe delay of $\leqslant 5$ ns.

The probe radiation (linewidth ~ 0.2 cm^{-1}) was stepped through the H-atom Doppler linewidth (typically ~ 2.5 cm^{-1}). At each step, an image deriving from a ''slice'' out of the full Doppler profile was accumulated from 10^3 laser firings. Each slice yielded a vertical strip at the detector, with different slices occupying different horizontal positions. The corresponding H-atom background image for each slice was recorded by putting the probe pulse before the pump pulse. The displayed images represent properly weighted superpositions of all of the background-subtracted slices (usually 20–50). This procedure works well because the angular distribution of the H-atoms is isotropic.

B. HRTOF

A schematic drawing of the HRTOF arrangement is given in Fig. 3. Details regarding the use of this method to obtain c.m. translational energy distributions for reaction (2) have been presented elsewhere.[22] Features of the HRTOF arrangement which differ significantly from those of the ion imaging arrangement are (i) its perpendicular molecular

TABLE I. HCO vibrational energies and their assignments in Fig. 5.

State $(\nu_1\nu_2\nu_3)$[a]	Energy[b]	Assignment in Fig. 5
(000)	···	a
(001)	1081	b
(010)	1868	c
(002)	2142	d
(100)	2435	e

[a] ν_1 = CH stretch, ν_2 = CO stretch, ν_3 = bend.
[b] Reference 32.

beam/detector geometry; (ii) the high-n Rydberg atom probe technique, in which the high-n Rydberg atoms are field ionized at a mesh a few mm in front of the MCP; and (iii) its long TOF path (~110 cm). The preparation of the molecular beam differed from that used in the ion imaging experiments,[22] resulting in a slightly higher parent rotational temperature ($T_{rot} \leqslant 10$ K). Photoexcitation was carried out by using photon energies ranging from 31 555.0 to 32 982.5 cm^{-1}. H-atom TOF spectra were recorded at those photon energies which yielded the largest signals; spectra were averaged over $>10^4$ laser firings.

III. RESULTS

For the photon energies employed in this study, the $S_1 \leftarrow S_0$ spectrum encompasses the region of the $1^1 4^3$, $2^3 4^1$, $2^2 4^3$, and $1^1 2^1 4^1$ S_1 vibronic levels; however, perturbations with other vibronic levels are too numerous to allow assignments.[30,31] Even with expansion cooling, the REMPI spectrum of formaldehyde shows that the excitation laser linewidth (i.e., $\leqslant 0.15$ cm^{-1} for both the imaging and HRTOF studies) is not sufficiently narrow to permit state-selective excitation at all photolysis wavelengths. Namely, some results derive from a single S_1 rovibronic level while others derive from two or more S_1 levels.

A. Ion imaging

Photofragment ion imaging data have been obtained at the following photon energies: 31 431.3, 31 554.6, 31 736.3, 32 248.6, 32 473.9, and 32 849.0 cm^{-1}; uncertainties are ± 0.5 cm^{-1}. To provide convenient figures-of-merit, the H+HCO dissociation energy (30 328.5 cm^{-1}) (Ref. 21) has been subtracted from the photon energies. The resulting numbers are the energies available for product excitations minus the parent rotational energies. The latter are not known for most of the transitions, but are modest on average because T_{rot} is $\leqslant 10$ K. Thus, these figures-of-merit are lower bounds to the available energies. They will be denoted $E^\dagger$ and rounded to the nearest wave number. The excitation energies have been chosen to lie just above the thresholds for the low lying HCO vibrational levels,[32] whose energies are given in Table I.

As mentioned above, the resolution is sufficient to identify HCO vibrational, but not rotational, excitations. Spatially isotropic product distributions are expected because dissociation is slow. Representative images are shown in Figs. 4(a) and 4(b) for $E^\dagger$ values of 2146 and 2521 cm^{-1}, respectively. The left-hand side shows the 2D projections of the 3D H-atom velocity distributions, while the right-hand side shows the corresponding 2D slices through the center of the reconstructed 3D distributions. The magnitude of the velocity increases with radial distance. Each 2D projection is a result of integrating over the H-atom Doppler line shape, as described in Sec. II. Symmetrized 2D images were used to generate 3D distributions via an Abel transform,[33] with the linear polarization of the photolysis radiation defining the symmetry axis. The vertical stripes in the images on the right hand side are due to noise which accumulates along the symmetry axis in the Abel transform. The velocity distributions corresponding to Figs. 4(a) and 4(b) are quite different. In (a), the intensity is skewed towards the inner and outer portions of the image, whereas in (b), four rings are observed, with intensity decreasing from the center.

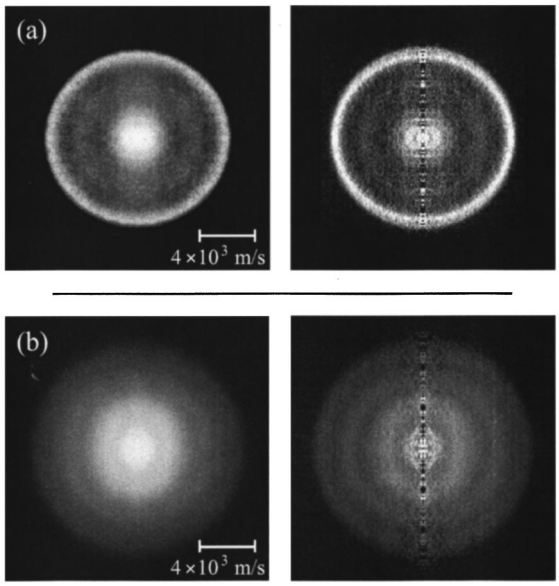

FIG. 4. Images of H atoms following H_2CO photodissociation at $E^\dagger$ values of (a) 2146 cm^{-1} and (b) 2521 cm^{-1}. Shown on the left are 2D *projections* of the 3D recoil velocity distributions (i.e., the raw data). The corresponding 2D *slices* through the symmetry axis of the reconstructed 3D intensity are shown on the right. Approximate velocity scales are included.

Figure 5 shows the HCO internal energy distributions (solid lines) obtained at the six $E^\dagger$ values. The features labeled a–e are attributed to HCO vibrational levels (Table I). For $E^\dagger$ values of 1408 and 2146 cm^{-1}, note the large HCO(000) population relative to the populations of the other HCO vibrational levels. The distributions at 1103, 1920, 2146, and 2521 cm^{-1} show HCO vibrations which are populated at energies near their thresholds, indicating the participation of a barrierless decomposition pathway.

The high sensitivity of ion imaging to fragments having slow recoil velocities can be seen by comparing the distributions given in Fig. 5 with the images given in Fig. 4. Though the fractions of HCO produced in highly excited vibrational levels is modest, the corresponding peaks in the intensity distributions of the 2D slices are large. This is because the slow ions, i.e., those which are associated with high internal excitations of the counter-fragment, lie near the center of the image, thus yielding a high ion density.

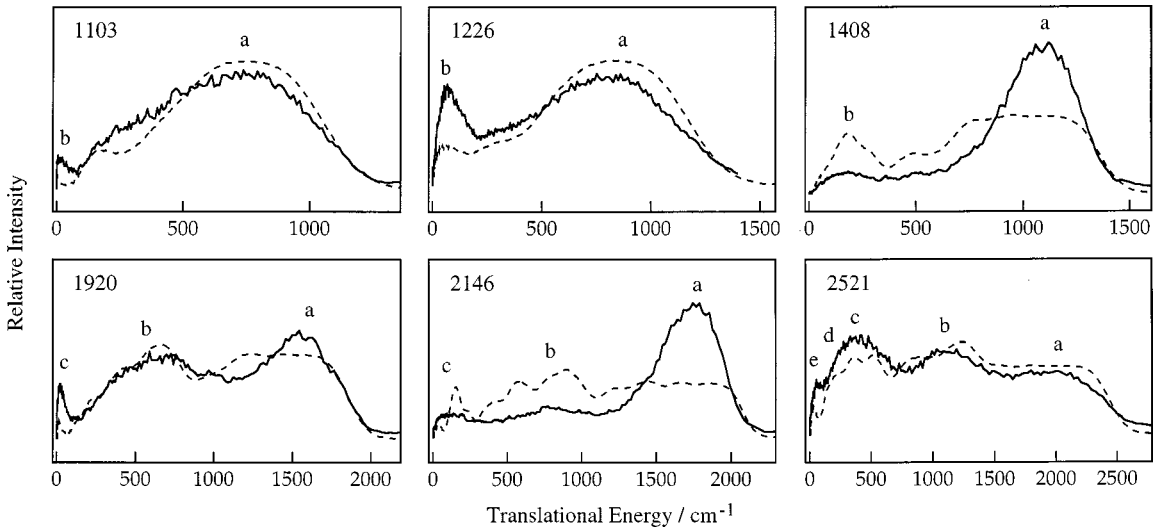

FIG. 5. Solid lines indicate H atom translational energy distributions obtained with the ion imaging apparatus. $E^{\dagger}$ values, in cm^{-1}, are indicated in the upper left hand sides of the boxes, and HCO vibrations are labeled a–e as per Table I. Fits using the SSE/PST model are indicated by the dashed lines. All distributions are normalized to the same area.

B. HRTOF

Figure 6 shows 40 HCO internal energy distributions obtained by using the HRTOF technique. The raw data have been transformed from the time domain to the energy domain. Whereas the S/N is not affected by the spontaneous emission lifetimes of the high-n Rydberg H atoms (which are a factor of ~50 larger than the longest flight times presented here, i.e., ~20 ms vs ~400 μs),[34] it is a decreasing function

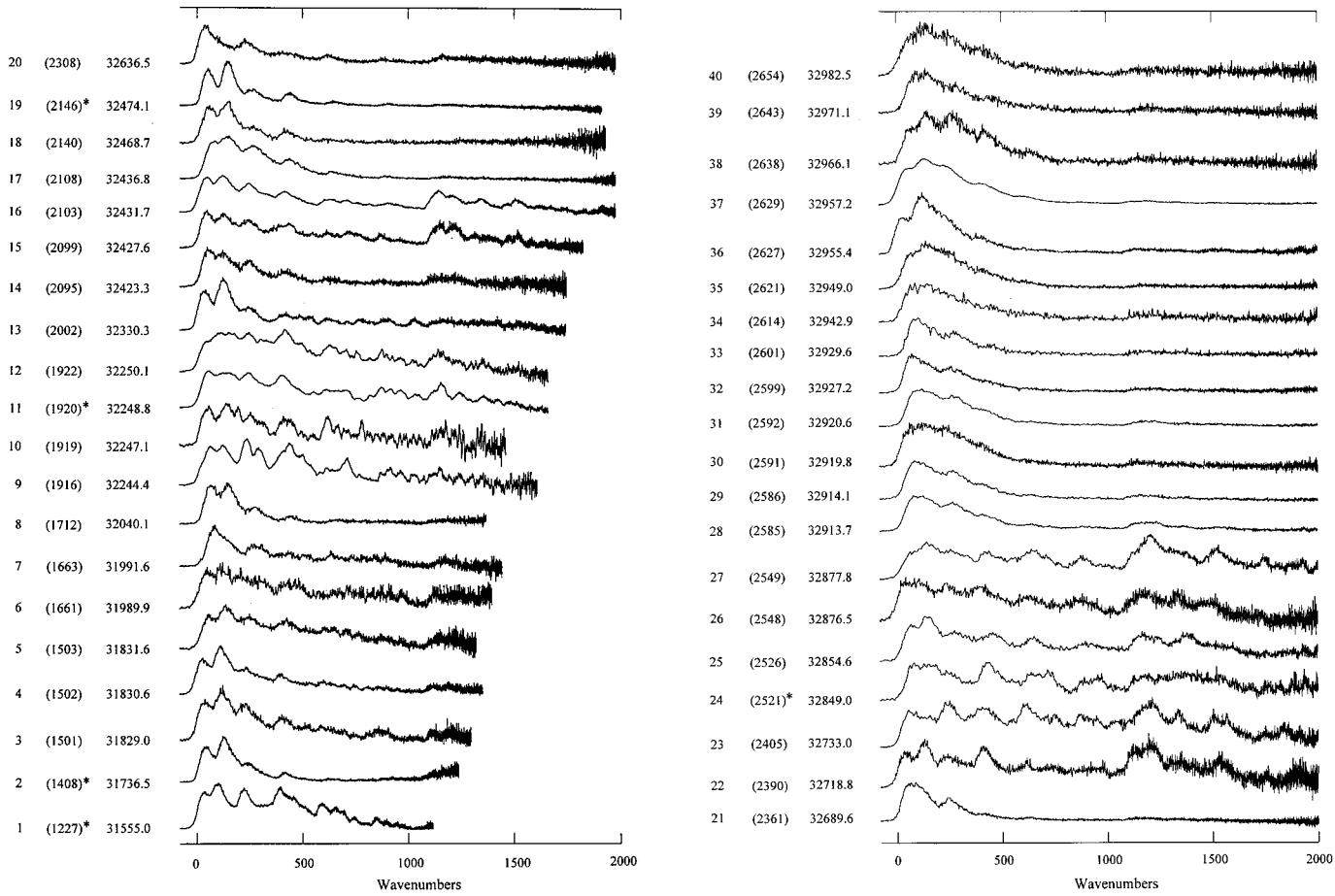

FIG. 6. HCO internal energy distributions obtained by using the HRTOF method. The distributions are numbered 1–40; photon energies and $E^{\dagger}$ values (parentheses) are in cm^{-1}. Asterisks denote traces for which ion imaging data were also collected. The distributions are scaled such that all HCO(000) $K_a = 1$ stacks have the same peak intensity.

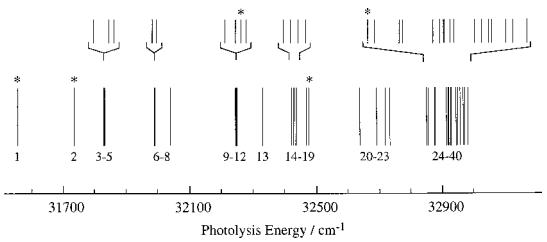

FIG. 7. Photolysis photon energies at which the HRTOF data were collected; asterisks and numeral designations as per Fig. 6. Congested regions are expanded.

of $E^\dagger$ due to the t^3 dependence of the Jacobian used to transform from the time domain to the energy domain. In addition, as the H-atom recoil speed in the H_2CO c.m. system approaches the speed of the molecular beam, the percentage of the H atoms that reach the detector diminishes, thereby distorting the distributions at the highest HCO internal energies.

Photon energies and $E^\dagger$ values (in parentheses) are listed beside each trace. The distribution of photon energies is shown in Fig. 7. HCO internal energy distributions obtained at wavelengths which were also used in the imaging studies are marked with asterisks in Fig. 6.

As shown in Fig. 8, K_a quantum numbers can be identified, where K_a is the quantum number for the projection of the angular momentum, N, on the HCO a-axis, with HCO approximated as a prolate symmetric top. [The A, B, and C rotational constants are 24.3, 1.5, and 1.4 cm^{-1}, respectively, for HCO(000), and 26.5, 1.5, and 1.4 cm^{-1} for HCO(001).[35,36]] The energies of the $K_a=N$ levels are marked by vertical lines. K_a values as high as 6 can be discerned in HCO(000) and HCO(001). In addition, Fig. 6 shows several traces that display structure which can be attributed to the distribution of the N quantum numbers within a K_a stack (e.g., trace 1, $K_a=5$ and 6). However, for the most part, the N distributions are structureless at the present resolution. Note that populations in HCO(000) levels having $K_a>6$ are difficult to discern, because these levels lie at the same energies as HCO(001) low-K_a levels. In addition, significant population of high-N levels smears out the K_a resolution for many of the distributions obtained at the highest photon energies (e.g., traces 30–35). In general, the rotational distributions fluctuate as the photon energy is changed, as has been reported previously at lower energies.[22]

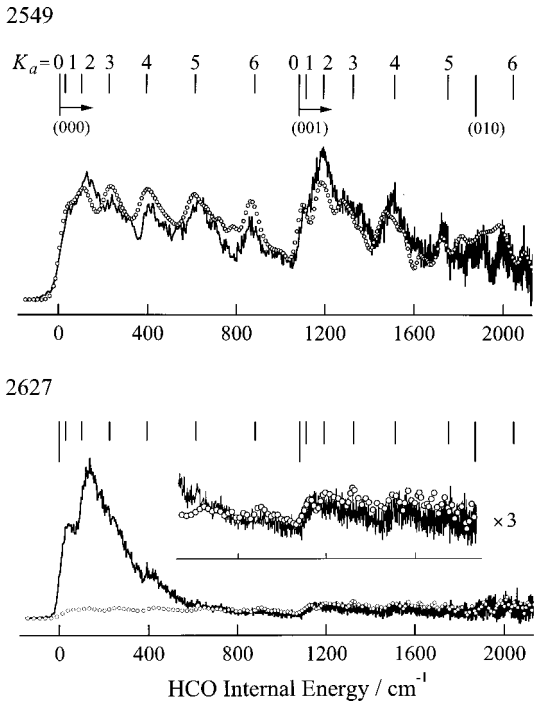

FIG. 8. HCO internal energy distributions for HRTOF data at $E^\dagger=2549$ and 2627 cm^{-1}. K_a stacks for the (000) and (001) vibrational levels are indicated for $K_a=N$. The 2549 cm^{-1} data show K_a values up to 6 for each vibrational level. Fits using the SSE/PST model are indicated by open circles; for $E^\dagger=2627$ cm^{-1}, the fit is scaled to the HCO(001) portion of the trace.

A careful examination of the distributions shown in Fig. 6 indicates that the signal intensity rises at the energy of the first excited HCO vibrational level (1080 cm^{-1}). In some cases this rise is prominent, while in others it is relatively small. However, it is always present. The presence of HCO(001) is interpreted as evidence for the persistent participation of the S_0 reaction channel, since vibrationally excited HCO is not expected to be produced via T_1 for the range of $E^\dagger$ values used in the present study.

IV. STATISTICAL MODEL

Because the S_0 pathway to H+HCO is barrierless, PSD's can be calculated straightforwardly by using statistical models. The separate statistical ensembles with phase space theory (SSE/PST) approach is an empirical method that has been shown to give good results for product excitations deriving from barrierless pathways in small polyatomics.[37–41] Therefore, it is applied here. This approach assumes that product vibrations (V) are determined earlier along the reaction coordinate than are product rotational, translational (R,T) degrees of freedom. Details are given elsewhere.[37]

The HCO vibrational distribution is obtained by using SSE, and the rotational distribution for a given HCO vibrational level is then calculated by using PST.[42] The long-range attractive potential is taken as $-C_6/r_{cm}^6$, where r_{cm} is the distance between the H atom and the HCO c.m. Adequate fits are obtained with C_6 values of $\sim 2\times10^{-78}$ J m^6. This value is similar to that used by Terentis *et al.* (i.e., $\sim 3\times10^{-78}$ J m^6),[43] who compared rotational distributions obtained at energies within 60 cm^{-1} of the reaction (2) threshold with results calculated by using statistical models. Because of the large uncertainties which arise due to the participation of T_1, fluctuation phenomena, etc., representing long-range attraction with a more accurate potential than the $-C_6/r_{cm}^6$ term provides no advantage in the present case. Though the conclusions presented below are not sensitive to details of the statistical model, constraints due to angular momentum conservation are significant, even at low excitation energies, because of the small reduced mass of this system.[44]

The intended use of the aforementioned statistical model is to help establish the respective contributions of the S_0 and T_1 reactive pathways. Because comparisons between calcu-

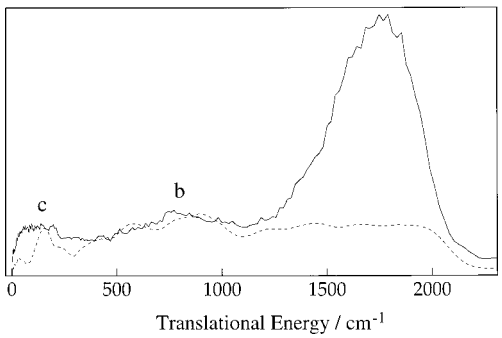

FIG. 9. Expanded view of the 2146 cm^{-1} trace taken from Fig. 5. The SSE/PST trace (dashed line) has been scaled by a factor of 0.4.

lated and experimental HCO distributions are subtle, only large differences are interpreted as strong evidence for T_1 participation. With this in mind, Fig. 5 shows comparisons between the ion imaging data (solid lines) and the statistical model (dashed lines). At $E^\dagger$ values of 1103, 1226, 1920, and 2521 cm^{-1} the fits are considered reasonable, so it is concluded that S_0 plays a major role.

On the other hand, at 1408 and 2146 cm^{-1}, the calculated distributions differ significantly from the experimental ones. In each case there is more population in HCO(000) than predicted by the statistical model. We interpret this to mean that reaction via T_1 is substantial, since the T_1 barrier is expected to channel energy into product *R,T* excitations (mainly *T*) but not HCO vibrational excitation. Population of excited HCO vibrational levels is attributed to reaction via S_0. For example, Fig. 9 shows a comparison for $E^\dagger = 2146\,cm^{-1}$, in which the calculated distribution for the S_0 pathway is scaled to the *b* and *c* features. In this case, both the S_0 and T_1 channels appear to be open, since the excited vibrational levels are incompatible with the T_1 pathway, while the large HCO(000) contribution is unlikely for the case of sole S_0 participation. The same conclusion may be drawn for the 1408 cm^{-1} trace (not shown) as well as for several additional distributions obtained by using the HRTOF method. Note that the HRTOF data taken at 2146 and 1408 cm^{-1} are in agreement with the ion imaging data.

The HRTOF data that display an S_0 signature (i.e., HCO vibrational excitation and rotational distributions extending to high K_a values) can also be simulated satisfactorily by using the same statistical model. Acceptable fits have been obtained by using C_6 values between 5×10^{-79} and $2\times10^{-78}\,J\,m^6$. Note that only regions where the c.m. translational energies exceed $\sim$ 500 cm^{-1} have been fit, because the signals here are believed to be proportional to populations, i.e., distortions of the distributions caused by the molecular beam velocity are small. In obtaining distributions from the data, the molecular beam velocity, photolysis volume, and temporal resolution are taken into account. For the range of recoil speeds encountered in the present study, $\Delta E/E$ is not constant, even for the faster fragments. A numerical model was used to estimate the resolution, which was then convoluted with the SSE/PST estimate to yield the calculated trace shown in Fig. 8.

Figure 8 shows the fits (circles) obtained by using $C_6 = 1.3\times10^{-78}\,J\,m^6$ for two representative distributions. At $E^\dagger = 2549\,cm^{-1}$, the K_a structure is reproduced for both the ground and excited vibrational levels, suggesting that S_0 dominates. On the other hand, at $E^\dagger = 2627\,cm^{-1}$, the experimental trace cannot be fit by using the model. However, when fitting the HCO(001) part of this trace, a fit is also obtained for the higher HCO(000) K_a levels, though the experimental S/N is very low. Thus, it appears that S_0 and T_1 both participate, with the latter producing significant amounts of rotationally cold HCO(000). Recall that only substantial T_1 participation can be identified.

In summary, the HRTOF and ion imaging data give consistent signatures of the S_0 and T_1 pathways. Furthermore, the ''best fit'' C_6 values are the same for both the HRTOF distributions and the ion imaging data obtained at the same $E^\dagger$ values.

V. DISCUSSION

At energies just above the H+HCO threshold, radical production occurs almost exclusively via the barrierless S_0 pathway because the T_1 barrier is high enough to inhibit reaction efficiently (Fig. 1). As the energy is increased from below to above the barrier, the T_1 pathway becomes increasingly important. The S_0 vs T_1 radical channel competition is dictated by the relative S_1 radiationless decay rates (i.e., $S_1 \rightarrow S_0$ vs $S_1 \rightarrow T_1$) because the rate for the molecular channel, which is open throughout the range of concern, is not strongly energy dependent.

A. S_1–S_0 coupling

Consider a single S_1 level coupled to a number of S_0 levels, which are in turn coupled to the S_0 dissociation continua. In the energy range of interest, the S_0 vibrational level density is $\sim 100/cm^{-1}$, which is divided equally between the four C_{2v} symmetry species. Because the $S_1(^1A_2) \leftarrow S_0(^1A_1)$ transition becomes allowed for vibronic states of B_2 symmetry, most of the strong transitions reach S_1 levels having odd numbers of ν_4 quanta (b_1 symmetry). These levels, in turn, can couple to S_0 vibrational levels of b_2 symmetry, i.e., those having odd numbers of quanta of ν_5 (the antisymmetric CH stretch) or ν_6 (the CH_2 rock). In the absence of Coriolis coupling, each symmetry species must be treated separately. However, Coriolis coupling mixes the vibrational symmetry species as well as the zeroth order K_a levels. Thus, a number of S_0 levels are accessible to a given S_1 level. In addition, the S_0 ''levels'' are quasibound, i.e., they are resonances whose widths are due to the sum of the unimolecular decay rates to the H_2+CO and H+HCO products. The coupling of S_1 and S_0 has been worked out, including ranges of values for the matrix elements.[6–10] However, this was done for D_2CO and it is not obvious how to scale the matrix element values obtained for D_2CO to the case of H_2CO.

The $S_1 \rightarrow S_0$ radiationless decay rates, as judged for example by the S_1 decay widths, are smaller than the sum of the S_0 unimolecular decay rates for the H_2+CO and H+HCO channels.[6] Thus, reaction rates cannot be inferred readily from S_1 decay widths. In addition, as mentioned earlier, there may be some lumpiness in the variation of the S_1–S_0 coupling strength with energy, because the averaging

which takes place over the S_0 resonances may be insufficient to completely eliminate all such structure. However, this is not expected to result in prominent effects, for example in PSD's. Note that at the energies of interest in the present study, S_0 unimolecular decomposition occurs in the regime of overlapping resonances.

B. S_1-T_1 coupling

The situation with S_1-T_1 coupling differs qualitatively from that of S_1-S_0 coupling. At the energies of interest, the T_1 vibrational level density is $\sim 0.3/\mathrm{cm}^{-1}$. This was estimated by using accurate experimental frequencies,[16] and when these were not available the best theoretical values.[23] Thus, the T_1 vibrational level density is sparse compared to that of S_0,[45] and above the T_1 barrier the T_1 resonance widths (which are due primarily to the H+HCO unimolecular decomposition channel) are much larger than the S_0 resonance widths. Also, as discussed before, a single S_1 level can couple to a number of zeroth-order T_1 rotational levels, each belonging to a different T_1 vibrational level.[11–13,22] Thus, the average separation between accessible T_1 resonances can be comparable to the T_1 resonance widths, even just above the top of the barrier.

The energy dependence of the contribution of T_1 to the decay of the S_1 levels is expected to be irregular in the region of the T_1 barrier. Note that below the T_1 barrier the resonances are sharp, because tunneling diminishes the reaction rates, and therefore S_1-T_1 coupling is more sporadic than either at or above the T_1 barrier. Thus, the energy of the T_1 barrier figures prominently in the competition between the S_0 and T_1 pathways. The most reliable value for the T_1 barrier comes from the recent *ab initio* calculation that place it at $1920\pm 210\,\mathrm{cm}^{-1}$,[23] in agreement with experimental results.[20] In combination with the data reported herein, it will be used to infer the reaction mechanism.

A series of spectroscopic studies by Ramsey and co-workers has shown that below the T_1 barrier the magnitudes of the S_1-T_1 matrix elements, $V_{S_1T_1}$, fluctuate, spanning the range 0.01–0.1 cm^{-1}.[16] These values can be used to make order-of-magnitude estimates of the $S_1\rightarrow T_1$ decay widths. For example, the width of an S_1 level decaying to the T_1 continuum via a single bound T_1 level is given in the weak $S_1\rightarrow T_1$ coupling limit by[46]

$$\hbar\Gamma_{S_1\rightarrow T_1}=|V_{S_1T_1}|^2\frac{\hbar\Gamma_{T_1}}{(E_{S_1}-E_{T_1})^2+(\hbar\Gamma_{T_1}/2)^2}, \tag{3}$$

where E_{S_1} and E_{T_1} are the energies of the bound S_1 and T_1 levels, and the unimolecular reaction of a T_1 level is characterized by its width, $\hbar\Gamma_{T_1}$. At resonance, Eq. (3) reduces to

$$\hbar\Gamma_{S_1\rightarrow T_1}=\frac{4|V_{S_1T_1}|^2}{\hbar\Gamma_{T_1}}. \tag{4}$$

For a T_1 vibrational level density of $0.3/\mathrm{cm}^{-1}$, the corresponding $1/h\rho$ value is $1.0\times 10^{11}\,\mathrm{s}^{-1}$. When substituting this for a typical value of Γ_{T_1} in Eq. (4), the range of $V_{S_1T_1}$ values reported by Ramsey and co-workers yields $\hbar\Gamma_{S_1\rightarrow T_1}$ values spanning 7.5×10^{-4} to $7.5\times 10^{-2}\,\mathrm{cm}^{-1}$. Thus, even at resonance, $\hbar\Gamma_{S_1\rightarrow T_1}$ can take on a large range of values.

Below the top of the T_1 barrier, the T_1 unimolecular decomposition rates are diminished by the tunneling probabilities. From Eq. (4), one sees that making $\hbar\Gamma_{T_1}$ narrower causes $\hbar\Gamma_{S_1\rightarrow T_1}$ to increase at exact resonance. However, as $\hbar\Gamma_{T_1}$ gets narrower, it becomes increasingly difficult to achieve the S_1-T_1 near-resonance condition of Eq. (4), and the net effect is that the average S_1-T_1 coupling is small, but should exhibit large fluctuations. This suggests that above the barrier, when $\hbar\Gamma_{T_1}$ increases and there are more opportunities for accessing these resonances, the contribution of the $S_1\rightarrow T_1$ pathway should increase, assuming sufficiently large $|V_{S_1T_1}|$ values. Given the coupling parameters of the present case, the energy range over which this occurs is expected to be broad and centered near the top of the T_1 barrier.

C. Experimental signatures

For the energy range under consideration (i.e., $1103 \leqslant E^{\dagger} \leqslant 2654\,\mathrm{cm}^{-1}$), reaction via T_1 is unlikely to result in a measurable amount of HCO vibrational excitation. Thus, HCO deriving from T_1 is expected to be almost entirely in the ground vibrational level. Since the calculated T_1 transition state geometry is such that the departing H atom is almost perpendicular to the HCO plane,[23] some *a*-axis rotation is inevitable. However the high K_a values (up to 6) seen in many of the spectra are unlikely to originate from reaction via a barrier. Specifically, the repulsive forces which act at distances beyond the barrier are expected to efficiently excite c.m. translation, and to a lesser extent b/c-axis rotation, which smears out the K_a structure at low K_a values.

On the other hand, reaction on S_0 to radical products occurs via a loose transition state, albeit with some tightening.[1] Thus, not only is HCO vibrational excitation anticipated at the energies of the present experiments, but according to statistical models, the HCO vibrational levels should be accessed at or just above their energy thresholds. HCO rotational excitation is also expected to be in reasonable accord with predictions made by using statistical models. For example, *a*-axis rotational excitation should be more abundant than in the case of reaction via T_1.

The above signatures are useful because the level distributions associated with the S_0 and T_1 pathways differ qualitatively. Were this not the case, fluctuations within S_0 and T_1 might mask the differences. Note that small T_1 contributions to the HCO PSD's can be concealed easily by S_0 fluctuations. Thus, T_1 is most readily identified when its relative population is substantial. On the other hand, small S_0 contributions can be identified by population of the highest energetically-allowed HCO vibrations.

Referring to the ion imaging data shown in Fig. 5, the distributions obtained at $E^{\dagger}=1103$, 1226, 1920, and 2521 cm^{-1} can be fit satisfactorily by using the statistical model, suggesting $S_1\rightarrow S_0$ dominance. In contrast, the distributions obtained at 1408 and 2146 cm^{-1} cannot be fit by using the statistical model. In particular, there is too little population in

the excited vibrational levels. It appears that the S_0 channel is open, as evidenced by some vibrational excitation, yet the T_1 contribution dominates. Note that 1408 cm^{-1} is below the calculated barrier height of $1920 \pm 210\ cm^{-1}$, suggesting tunneling and the existence of near resonance with a specific T_1 level.

Similar conclusions are reached by inspection of the HRTOF spectra. Referring to Fig. 6, the HRTOF data display features that can be ascribed to S_0 and T_1. For example, at the highest $E^\dagger$ values (2585–2654 cm^{-1}) the distributions display a small contribution from HCO(001). Also, within HCO(000), *a*-axis rotation is modest, whereas more *b*/*c*-axis rotation is present than in most of the other distributions. Thus, these distributions display T_1 signatures.

On the other hand, the distributions obtained between 2390 and 2549 cm^{-1} are different. There is more HCO(001), more *a*-axis rotation, and better resolution of the K_a peaks. However, at 2361 cm^{-1} a T_1 signature appears and persists as $E^\dagger$ is lowered to 2108 cm^{-1}. Below there, the S_0 signature dominates, but not without exception, e.g., 1408 cm^{-1}.

Because of the overlap of the reactive resonances on S_0 at the energies of concern, it is expected that the rate associated with this channel varies more smoothly with energy than does the rate associated with the T_1 channel. The latter fluctuates because the triplet resonances are not strongly overlapped throughout the range of interest. The calculated T_1 barrier height of $1920 \pm 210\ cm^{-1}$ is consistent with this interpretation. Near and below the top of the T_1 barrier, S_0 dominates on average, whereas above this energy T_1 plays the more significant role. We believe that the data shown in Figs. 5 and 6 are a representative sampling for the range $1103 \leqslant E^\dagger \leqslant 2654\ cm^{-1}$.

D. Relation to previous studies

The present data are relevant to previous experimental observations. For example, it has been pointed out that at higher energies T_1 may dominate.[22] Thus, the nonstatistical HCO vibrational distributions measured at photon energies of $\sim 34\,000\ cm^{-1}$ by Reilly *et al.*,[47] in which nearly two-thirds of the HCO molecules are in HCO(000), may be the result of triplet dominance. However, at these energies, triplet surfaces other than T_1 may also participate.

The present work is also relevant to the study of van Zee *et al.*,[48] which examines the possibility of a second molecular channel opening in the vicinity of the radical channel threshold. The proposed mechanism invokes radical dissociation that ''almost occurs,'' i.e., large H–HCO distances are accessed. These large distances facilitate H-atom abstraction. Thus, a ''self-reaction'' occurs, producing the observed increase in the fraction of CO($v=0$, low-J) fragments at excess energies within $\sim 1500\ cm^{-1}$ of the radical threshold. The dynamics on the S_0 surface which produces HCO *a*-axis rotation (with K_a values extending to 5 and 6) may support such a mechanism, namely, the high *a*-axis angular velocity and the counter-rotating HCO–H motion.

VI. SUMMARY

Photoinitiated $S_1 \rightarrow S_0$ and $S_1 \rightarrow T_1$ pathways to H+HCO products have been examined experimentally in the region $1103 \leqslant E^\dagger \leqslant 2654\ cm^{-1}$. Complementary experimental techniques (ion imaging and HRTOF) have been used to obtain c.m. translational energy distributions, which mirror the corresponding HCO internal energy distributions.

The S_0 pathway leading to H+HCO is barrierless, whereas the T_1 barrier height has been calculated to be $1920 \pm 210\ cm^{-1}$ relative to the H+HCO threshold.[23] Consequently, S_0 dissociation is expected to dominate at energies above the H+HCO threshold but below the top of the barrier, while T_1 dissociation is expected to dominate well above the top of the barrier. S_0 and T_1 signatures differ qualitatively; S_0 yields near statistical PSD's, whereas T_1 is expected to yield HCO having no measurable vibrational excitation and relatively little *a*-axis rotation.

The data display both the S_0 and T_1 signatures and demonstrate the complexity of the reaction dynamics throughout the region where T_1 turns on. It is seen that at the highest $E^\dagger$ values T_1 dominates, though there is a persistent S_0 contribution, as evidenced by the presence of the HCO(001) vibrational level in all of the PSD's. At the lowest $E^\dagger$ values, S_0 dominates, though T_1 contributions appear sporadically. Fluctuations are expected to be present, with T_1 participation being infrequent at the lower energies and prevalent (but not to the total exclusion of S_0) at the higher energies. These observations are consistent with the calculated value of the T_1 barrier height,[23] as well as the earlier study of Chuang *et al.*[20]

The transition from S_0 to T_1 dominance occurs over a broad energy range extending from below to above the calculated top of the T_1 barrier. There is no abrupt break where channel switching occurs, for example at the barrier top. Below the barrier top, T_1 participation is observed and attributed to tunneling, while just above it, the T_1 resonances are not sufficiently dense to dominate. However, as the energy is increased to the highest values used in the present study, T_1 dominance becomes clear, though even here S_0 is present to a modest extent. It is likely that such behavior is not limited to H_2CO, and that these or similar considerations should be taken into account whenever competitive reaction pathways are accessed via radiationless decay.

ACKNOWLEDGMENTS

This research was supported by the U.S. Department of Energy Contracts Nos. DE-FG-03-88ER13959 (H.R.) and DE-FG-03-85ER13363 (C.W.). We wish to thank Ilya Bezel for many insightful discussions.

[1] W. H. Green, C. B. Moore, and W. F. Polik, Annu. Rev. Phys. Chem. **43**, 591 (1992).
[2] C. B. Moore and J. C. Weisshaar, Annu. Rev. Phys. Chem. **34**, 525 (1983).
[3] E. K. C. Lee and R. S. Lewis, Adv. Photochem. **12**, 1 (1980).
[4] W. H. Miller, J. Am. Chem. Soc. **101**, 6810 (1979).
[5] S. K. Gray, W. H. Miller, Y. Yamaguchi, and H. F. Schaefer, J. Am. Chem. Soc. **103**, 1900 (1981).
[6] W. F. Polik, D. R. Guyer, W. H. Miller, and C. B. Moore, J. Chem. Phys. **92**, 3471 (1990).

[7] W. F. Polik, C. B. Moore, and W. H. Miller, J. Chem. Phys. **89**, 3584 (1988).
[8] D. R. Guyer, W. F. Polik, and C. B. Moore, J. Chem. Phys. **84**, 6519 (1986).
[9] R. Hernandez, W. H. Miller, C. B. Moore, and W. F. Polik, J. Chem. Phys. **99**, 950 (1993).
[10] W. H. Miller, R. Hernandez, C. B. Moore, and W. F. Polik, J. Chem. Phys. **93**, 5657 (1990).
[11] C. G. Stevens and J. C. D. Brand, J. Chem. Phys. **58**, 3324 (1973).
[12] J. C. D. Brand and C. G. Stevens, J. Chem. Phys. **58**, 3331 (1973).
[13] J. C. D. Brand and D. S. Liu, J. Phys. Chem. **78**, 2270 (1974).
[14] R. G. Miller and E. K. C. Lee, J. Chem. Phys. **68**, 4448 (1979).
[15] D. J. Clouthier, A. M. Craig, and D. A. Ramsay, Can. J. Phys. **61**, 1073 (1983).
[16] D. J. Clouthier and D. A. Ramsay, Annu. Rev. Phys. Chem. **34**, 31 (1983).
[17] H.-L. Dai, R. W. Field, and J. L. Kinsey, J. Chem. Phys. **82**, 1606 (1984).
[18] W. M. Gelbart, M. L. Elert, and D. F. Heller, Chem. Rev. **80**, 403 (1980).
[19] M. L. Elert, Ph.D. thesis, University of California at Berkeley, 1977.
[20] M.-C. Chuang, M. F. Foltz, and C. B. Moore, J. Chem. Phys. **87**, 3855 (1987).
[21] A. C. Terentis and S. H. Kable, Chem. Phys. Lett. **258**, 626 (1996).
[22] M. J. Dulligan, M. F. Tuchler, J. Zhang, A. Kolessov, and C. Wittig, Chem. Phys. Lett. **276**, 84 (1997).
[23] Y. Yamaguchi, S. S. Wesolowski, T. J. V. Huis, and H. F. Schaefer, J. Chem. Phys. **108**, 5281 (1998).
[24] D. W. Chandler and P. L. Houston, J. Chem. Phys. **87**, 1445 (1987).
[25] A. J. R. Heck and D. W. Chandler, Annu. Rev. Phys. Chem. **46**, 335 (1995).
[26] D. H. Parker and A. T. J. B. Eppink, J. Chem. Phys. **107**, 2357 (1997).
[27] A. T. J. B. Eppink and D. H. Parker, Rev. Sci. Instrum. **68**, 3477 (1997).
[28] T. Droz-Georget, M. Zyrianov, and H. Reisler, Chem. Phys. Lett. **276**, 316 (1997).
[29] A. Clark, C. Kosmidis, K. W. D. Ledingham, A. Marshall, J. Sander, R. P. Singhai, and M. Campbell, Chem. Phys. Lett. **26**, L665 (1993).
[30] V. Seutherman, V. A. Job, and K. K. Innes, J. Mol. Spectrosc. **33**, 189 (1970).
[31] V. A. Job, V. Seutherman, and K. K. Innes, J. Mol. Spectrosc. **30**, 365 (1969).
[32] J. D. Tobiason, J. R. Dunlop, and E. A. Rohlfing, J. Chem. Phys. **103**, 1448 (1995).
[33] R. N. Bracewell, *The Fourier Transform and its Applications* (McGraw–Hill, New York, 1986).
[34] L. Schnieder, K. Seekamp-Rahn, F. Liedeker, H. Steuwe, and K. H. Welge, Faraday Discuss. Chem. Soc. **91**, 259 (1991).
[35] G. A. Blake, K. V. L. N. Sastry, and F. C. DeLucia, J. Chem. Phys. **80**, 95 (1984).
[36] J. M. Brown and D. A. Ramsay, Can. J. Phys. **53**, 2232 (1975).
[37] C. Wittig, I. Nadler, H. Reisler, M. Noble, J. Catanzarite, and G. Radhakrishnan, J. Chem. Phys. **83**, 5581 (1985).
[38] I. Nadler, M. Noble, H. Reisler, and C. Wittig, J. Chem. Phys. **82**, 2608 (1985).
[39] C. X. W. Qian, M. Noble, H. Reisler, and C. Wittig, J. Chem. Phys. **83**, 5573 (1985).
[40] E. A. Wade, H. Clauberg, S. K. Kim, A. Mellinger, and C. B. Moore, J. Phys. Chem. A **101**, 732 (1997).
[41] E. A. Wade, A. Mellinger, M. A. Hall, and C. B. Moore, J. Phys. Chem. **101**, 6568 (1997).
[42] P. Pechukas and J. C. Light, J. Chem. Phys. **42**, 3281 (1965).
[43] A. C. Terentis, S. E. Waugh, G. F. Metha, and S. H. Kable, J. Chem. Phys. **108**, 3187 (1998).
[44] M. Zyrianov, A. Sanov, T. Droz-Georget, and H. Reisler, J. Chem. Phys. **110**, 10774 (1999).
[45] A. C. Luntz and V. T. Maxson, Chem. Phys. Lett. **26**, 553 (1974).
[46] C. Cohen-Tannoudji, J. Dupont-Roc, and G. Grynberg, *Atom–Photon Interactions* (Wiley, New York, 1992).
[47] J. P. Reilly, J. H. Clark, C. B. Moore, and G. C. Pimentel, J. Chem. Phys. **69**, 4381 (1978).
[48] R. D. v. Zee, M. F. Foltz, and C. B. Moore, J. Chem. Phys. **99**, 1664 (1993).